Nanoscale

ROYAL SOCIETY OF CHEMISTRY

MINIREVIEW

View Article Online
View Journal | View Issue

Cite this: *Nanoscale*, 2020, **12**, 20141

Interfacial control and design of conductive nanomaterials for transparent nanocomposite electrodes

Yongkwon Song and Jinhan Cho *

A few critical issues in preparing transparent conductive electrodes (TCEs) based on solution-processable conductive nanomaterials are their low electrical conductivity and the unfavorable trade-off between electrical conductivity and optical transparency, which are closely related to the organic ligands bound to the nanomaterial surface. In particular, bulky/insulating organic ligands bound to the surface of conductive nanomaterials unavoidably act as high contact resistance sites at the interfaces between neighboring nanomaterials, which adversely affects the charge transfer kinetics of the resultant TCEs. This article reviews the latest research status of various interfacial control approaches for solution-processable TCEs. We describe how these approaches can be effectively applied to conductive nanomaterials and how interface-controlled conductive nanomaterials can be employed to improve the electrical and/or electrochemical performance of various transparent nanocomposite electrodes, including TCEs, energy storage electrodes, and electrochromic electrodes. Last, we provide perspectives on the development direction for next-generation transparent nanocomposite electrodes and breakthroughs for significantly mitigating the complex trade-off between their electrical/electrochemical performance and optical transparency.

Received 14th August 2020,
Accepted 8th September 2020

DOI: 10.1039/d0nr05961g

rsc.li/nanoscale

1. Introduction

Transparent conductive electrodes (TCEs) play a pivotal role in preparing a variety of transparent electronics such as displays, touch screens, sensors, organic/inorganic light-emitting

Department of Chemical and Biological Engineering, Korea University, 145 Anam-ro, Seongbuk-gu, Seoul 02841, Republic of Korea. E-mail: jinhan71@korea.ac.kr

Yongkwon Song

Yongkwon Song is a Ph.D. candidate under Prof. Jinhan Cho at the Department of Chemical and Biological Engineering in Korea University. His research interest currently focuses on the preparation of functional nanocomposite electrodes based on the interfacial control of metal and/or metal oxide nanomaterials and layer-by-layer assembly.

Jinhan Cho

Jinhan Cho is a professor at the Department of Chemical and Biological Engineering in Korea University since 2010. He received a Ph.D. degree in Chemical Engineering from Seoul National University (2001). He did postdoctoral courses at the Max Planck Institute of Colloids and Interfaces (2001–2002) and the University of Melbourne (2003). He was a senior researcher at LG Chemistry R&D center (2003–2005) and joined the School of Materials Science and Engineering at Kookmin University (2006–2010). He has expertise in the surface modification of nanomaterials as well as in the layer-by-layer-assembled functional multilayers, including optical films, nonvolatile memory devices, and energy storage/harvesting devices.

diodes (LEDs), photovoltaics, energy storage devices, and smart windows.[1–10] Currently, transparent conducting oxides (TCOs), such as indium tin oxide (ITO), fluorine-doped tin oxide (FTO), and aluminum-doped zinc oxide (AZO), have been widely employed as conductive materials in TCEs due to their excellent opto-electrical properties (*i.e.*, high optical transparency above ~80% at a low sheet resistance of 10–100 Ω sq^{-1}) and satisfactory operational stability in air.[11–18] For example, in the case of commercial ITO electrodes that have been the most widely used in the TCE industries, ITOs are deposited onto transparent glass substrates through energy-intensive vacuum deposition processes (mainly sputtering).[13–18] Then, the formed ITO films are annealed at high temperatures under a reducing atmosphere to promote crystallization and to increase the ratio of oxygen vacancies in the ITOs.[13,14] It is well known that these oxygen vacancies act as n-type dopants in ITOs, transforming insulating oxides into semiconducting oxides, which has a significant effect on the electrical conductivity of the ITO electrodes.[13,19–21]

However, conventional vacuum deposition processes reported to date intrinsically possess a few critical drawbacks: (i) the low production yield of only 15–30% despite the high cost of target materials; (ii) the electrode size that is defined by the size of highly expensive vacuum chambers; (iii) the incompatibility with complex geometric substrates such as high-curvature substrates; and (iv) the lack of flexibility owing to the brittleness of sputtered bulk films.[6,14–18] These limitations create obstacles in realizing the large-scale production of TCEs with the desired geometries and flexibilities. Although graphene films grown by chemical vapor deposition (CVD) processes may be one of attractive candidates for TCEs, their extremely high synthesis temperature (~1000 °C) limits the versatility of TCEs.[7,22,23] Additionally, metal nanomesh-based films with patterned metal lines can also exhibit good optical and electrical properties (sheet resistance ~5–100 Ω sq^{-1}; optical transparency >80%).[24–28] However, in most cases, these films require a relatively complicated patterning process, such as photolithography, nanosphere lithography or grain boundary lithography.[25–28] Furthermore, metal nanomesh-based films with numerous open holes are restrictively applied to touch panels or sensors, possibly allowing a large interdistance (>10 μm) between adjacent metal lines.[6,18]

On the other hand, solution process-based approaches are promising in terms of more effective deposition for the large-scale preparation of TCEs with various sizes and geometries compared to the abovementioned traditional vacuum or dry deposition processes. For example, solution-processable TCO films can be prepared using a sol–gel method based on the hydrolysis of molecular precursors (*i.e.*, metal salts or alkoxides) and the polycondensation of metal hydroxides.[29,30] Although it has been reported that sol–gel-derived TCO films can exhibit a high opto-electrical performance comparable to sputtered TCO films, prolonged annealing processes at high temperatures (>450 °C) are needed to promote both the crystallization and the thermal decomposition of large amounts of residual organic compounds in the TCO films.[31,32]

Instead of sol–gel precursors, a variety of solution-processable conducting polymers (*e.g.*, poly(3,4-ethylenedioxythiophene:polystyrene sulfonate (PEDOT:PSS)) or carbon-based materials (*e.g.*, carbon nanotubes (CNTs) and reduced graphene oxides (r-GOs)) can be directly used for the preparation of TCEs.[23,33–36] However, their low electrical conductivity and light absorption properties (sheet resistance >100 Ω sq^{-1}; optical transparency >80%) act as major obstacles to the preparation of high-performance TCEs.[18,24] As an alternative, solution-processable TCO nanoparticles (NPs), metal NPs, and metal nanowires (NWs) have also been applied to TCEs using spin coating, spray coating, drop casting, doctor blading, Meyer rod coating, layer-by-layer assembly, printing, and roll-to-roll deposition methods.[6,15–18] For these approaches, high-quality conductive nanomaterials (*i.e.*, high crystallinity and uniform size/shape) have been synthesized using relatively bulky organic ligands.[37–40] However, these bulky organic ligands bound to the surface of nanomaterials increase the separation distance between adjacent nanomaterials and operate as insulating barriers (*i.e.*, contact resistance sites) within the assembled electrodes.[41–49] Consequently, the presence of bulky/insulating organic ligands substantially impedes electron transport at the interfaces between neighboring conductive nanomaterials. Particularly, in the case of preparing TCEs using spherical-type TCO NPs, the effects of the contact resistance on the electrical performance of TCEs become much more important due to the large contact area formed at the NP–NP interfaces.[50] Additionally, if reduction processes at high temperatures are carried out to induce more closely packed TCO NP films and/or increase the oxygen vacancies in the TCO NP films,[42–44] partially decomposed hydrocarbon-based ligands can cause light absorption in the visible wavelength range due to the formation of carbon ashes, which can then decrease the optical transparency of TCO NP-based TCEs.[21] Therefore, interfacial control of conductive nanomaterials, involving the effective removal and/or proper exchange of bulky/insulating organic ligands on the surface of nanomaterials, can provide a fundamental solution to achieve the desired optical/electrical performance of conductive NP (or NW)-based TCEs.

Along with critical issues related to organic ligands, the shapes and/or chemical properties of conductive nanomaterials should be considered for the preparation of high-performance TCEs. Specifically, in the case of one-dimensional (1D)-conductive metal NW films with randomly percolating networks, the formation of vacant and nonconductive domains improves the light transmission but results in an extremely narrow electrode area with a rough surface.[5,51–54] Consequently, highly porous metal NW films have the limited contact area between TCEs and upper active layers and the risk of short circuits in charge injection applications such as LEDs and photovoltaics.[53] Furthermore, Ag or Cu NW films have a low operational stability under ambient and/or electrochemical conditions due to their irreversible byproduct reactions with the moisture, oxygen, and sulfur-containing compounds in air and/or with reactive ions in electrolytes.[55–57] Therefore, metal

NW films often require an additional coating of other materials for surface planarization and/or protection to ensure facile charge transfer from the entire electrode area to the active layers along with an extremely smooth surface morphology.[52–58] For example, it has been reported that the coating of PEDOT:PSS or TCO layers onto metal NW films can contribute to the reduction of surface roughness and/or the improvement of chemical stability of the metal NW films.[52–56] However, it should be noted that the coating of insulating materials can inevitably hinder the charge transport from the TCEs to the active layers (*i.e.*, in the device structure composed of TCEs/insulating materials/active layers).[57,58]

Interfacial control and design are also important factors in determining the performance in other transparent electrochemical applications, including energy storage and electrochromic (EC) devices. Specifically, when a variety of transition metal oxide (TMO) nanomaterials (*e.g.*, manganese oxide (MnO_x), iron oxide (FeO_x), and cobalt oxide (CoO_x) NPs for energy storage properties; tungsten oxide (WO_x) and molybdenum oxide (MoO_x) nanorods (NRs) for EC properties) are exploited for electrochemical electrodes with the desired functionalities, bulky organic ligands on the surface of NPs (or NRs) severely limit the charge transfer between neighboring NPs and further obstruct the facile access of reactive ions to the NP surface for electrochemical reactions.[59–63] As a result, the high contact resistance occurring from organic ligands at the TMO NP–NP interfaces as well as the inherently low electrical conductivity of TMO NPs leads to the poor electrochemical performance of electrodes.[59,64] Therefore, it is desirable that conductive nanomaterials are additionally incorporated into TMO NP films for facile charge transport within the electrodes.[59–61,65–68] However, simple insertion or blending without special consideration of interfacial interactions between TMO NPs and conductive nanomaterials can induce phase segregations or agglomerations.[69] Moreover, the excessive use of conductive nanomaterials with strong light absorption, such as CNTs or r-GOs, can have an adverse effect on the optical transparency of electrodes.[66–68] To address these problems and further improve the overall electrical and/or electrochemical performance of transparent nanocomposite electrodes without a notable loss in optical transparency, conductive nanomaterials with minimal light absorption, such as TCO NPs, should be uniformly incorporated into TMO NP films through elaborate interfacial interactions.

Recently, it has been reported that various hydrophobic organic ligands (*e.g.*, oleic acid (OA), oleylamine (OAm), and tetraoctylammonium (TOA)) on the surface of metal and/or metal oxide NPs can be easily substituted with amine (NH_2)- or carboxylic acid (COOH)-functionalized linkers during ligand replacement layer-by-layer (LR-LbL) assembly in organic media.[59–61,70–77] Particularly, consecutive ligand replacements by small molecular linkers with extremely low molecular weights (M_w) can significantly reduce the contact resistance by minimizing the separation distance between adjacent NPs, which can enhance the charge transport at the NP–NP interfaces.[74–77] Additionally, it has also been demonstrated that the uniform and stable incorporation of conductive NPs into LbL-assembled nanocomposite films can be achieved through the use of linkers that can directly bridge adjacent NPs.[59–61] That is, LR-LbL assembly using small molecular linkers in organic media enables the preparation of highly optimized nanocomposite electrodes with regard to charge transfer efficiency, outperforming conventional LbL assembly (mainly electrostatic LbL assembly in aqueous media).[75–77]

In this minireview, we introduce various interfacial control approaches for conductive nanomaterials and review their successful applications in TCEs, transparent energy storage, and EC devices (Fig. 1). We highlight that research works demonstrating the importance of interfacial control have been scarcely reviewed despite the presence of numerous reviews related to conductive nanomaterials and their applications to TCEs. First, we briefly discuss conductive nanomaterials used for the preparation of TCEs and then describe the recently reported interfacial approaches, including electrochemical desorption, chemical desorption, electrostatic LbL assembly, and LR-LbL assembly (section 2). Next, we explore the potential utilization of interface-controlled TCO NPs for facile charge transfer within TMO NP-based transparent supercapacitor and EC electrodes (section 3). Finally, we provide an overall summary and perspectives on interfacial engineering for developing a variety of next-generation transparent nanocomposite electrodes (section 4).

2. Interfacial control approaches of conductive nanomaterials for TCEs

2.1 Electrochemical desorption-based interfacial control

1D metal NWs with a large aspect ratio have been recognized as one of attractive conductive nanomaterials for the preparation of TCEs by virtue of the superior electrical and mechanical properties as well as the formation of efficient junctions among metal NWs.[78–80] Randomly percolating networks of metal NW films with numerous open holes can ensure both high electrical conductivity and light transmission, which can be controlled by the loading amount of NWs on the substrates.[81] In particular, Ag NWs have been intensively studied due to their facile synthesis with scalability and reproducibility compared to other metal NWs, such as Au NWs or Cu NWs.[82] The most widely used and well-established synthesis method of Ag NWs is polyol reduction, involving the reduction of Ag ions in the presence of polyvinylpyrrolidone (PVP) ligands.[83–85] In this case, the PVP ligands play important roles as steric stabilizers and structure-directing agents that allow the anisotropic growth of Ag NWs by selectively adsorbing on the (100) facets of Ag nuclei.[86] Despite the importance of PVP ligands, the presence of bulky/insulating PVP ligands, which have strong coordination bonds with the Ag NW surface *via* carbonyl groups, limits the preparation of highly conductive Ag NW films.[87] Therefore, the synthesized Ag NWs require many repetitive washing and additional treatment processes (*e.g.*, thermal, plasmonic, and plasma treatments) to remove the

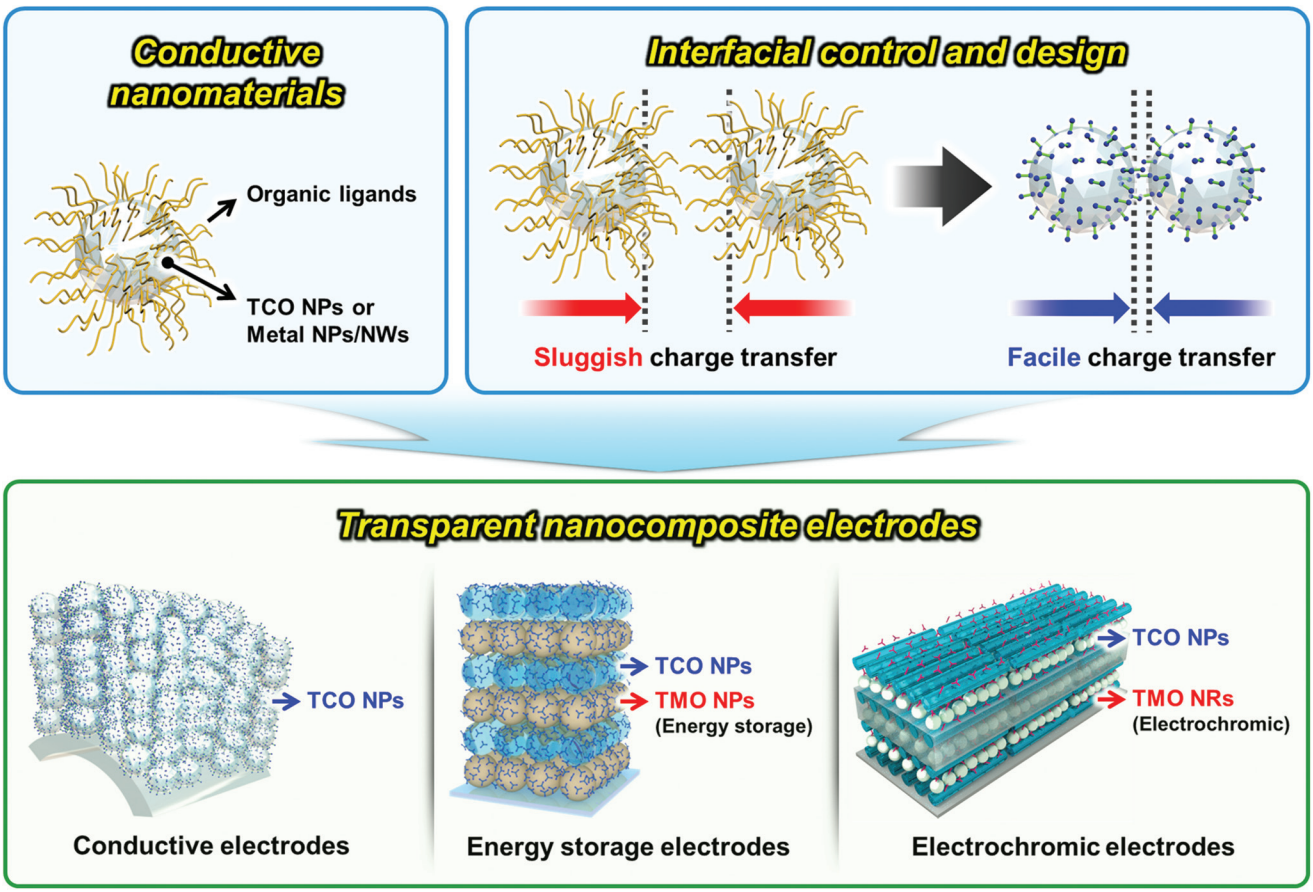

Fig. 1 Schematic illustration of the interfacial control of conductive nanomaterials for the preparation of transparent nanocomposite electrodes with facile charge transport. Reproduced with permission.[123] Copyright 2020, Wiley-VCH. Reproduced with permission.[124] Copyright 2019, American Chemical Society. Reproduced with permission.[125] Copyright 2019, The Royal Society of Chemistry.

PVP ligands and/or to decrease the contact resistance within the assembled Ag NW films.[88–92]

Recently, a variety of unique interfacial approaches for removing residual PVP ligands adsorbed on the surface of Ag NWs have been reported by a few research groups. For example, Duan and coworkers reported electrochemical cleaning that can induce the desorption of PVP ligands present in Ag NW films using the hydrogen evolution reaction (HER).[87] When the spin-coated Ag NW films were polarized in the HER potential region, the formation of Ag–H bonds induced the rapid desorption of PVP ligands due to the higher strength of Ag–H bonds (170 kJ mol^{-1}) than that of Ag–O coordination bonds (50.9 kJ mol^{-1}) of PVP ligands (Fig. 2a). Then, the H atoms bound to the Ag surface were converted into H_2 bubbles, pushing away the detached PVP ligands. These HER behaviors were confirmed in the cyclic voltammetry (CV) curves with the increasing cycle number (Fig. 2b). The potential value at the same current densities gradually shifted toward a more positive potential, indicating that the overpotential for the HER decreased as the electrochemically active Ag NW surface was exposed by the removal of PVP ligands. Additionally, the neatly cleaned surface of Ag NWs was also observed through electron microscopy analysis (Fig. 2c). Consequently, the surface-cleaned Ag NW films showed a low sheet resistance of 13 Ω sq^{-1} with a high transmittance of 90.9% at a wavelength of 550 nm by significantly lowering the contact resistance at the NW–NW junctions (Fig. 2d).

Fang *et al.* also demonstrated that electrochemical etching can produce ligand-free Ag NW films while tailoring the diameter of NWs.[93] The well-regulated electrochemical reactions at low current densities caused the dissolution of the outermost Ag atoms along with the removal of PVP ligands within blade-coated Ag NW films (Fig. 2e). In this case, the optical/electrical properties (*i.e.*, haze, transmittance, and sheet resistance) of the Ag NW films were modulated according to the diameter of the Ag NWs (Fig. 2f and g). Specifically, a decrease in the diameter of Ag NWs led to high optical transmittance and low haze due to the decreased shadow area. More interestingly, the sheet resistance of Ag NW films was notably decreased after etching, although the individual resistance of Ag NWs increased due to the narrowed conductive pathway (Fig. 2e and g). These improved electrical properties of Ag NW films were mainly attributed to the removal of bulky/insulating PVP ligands as well as metallic fusion (or welding) at the ligand-free Ag NW–NW junctions. Since the activation energy of Ag atoms for diffusion is lower than 1 eV, the migration of Ag atoms between

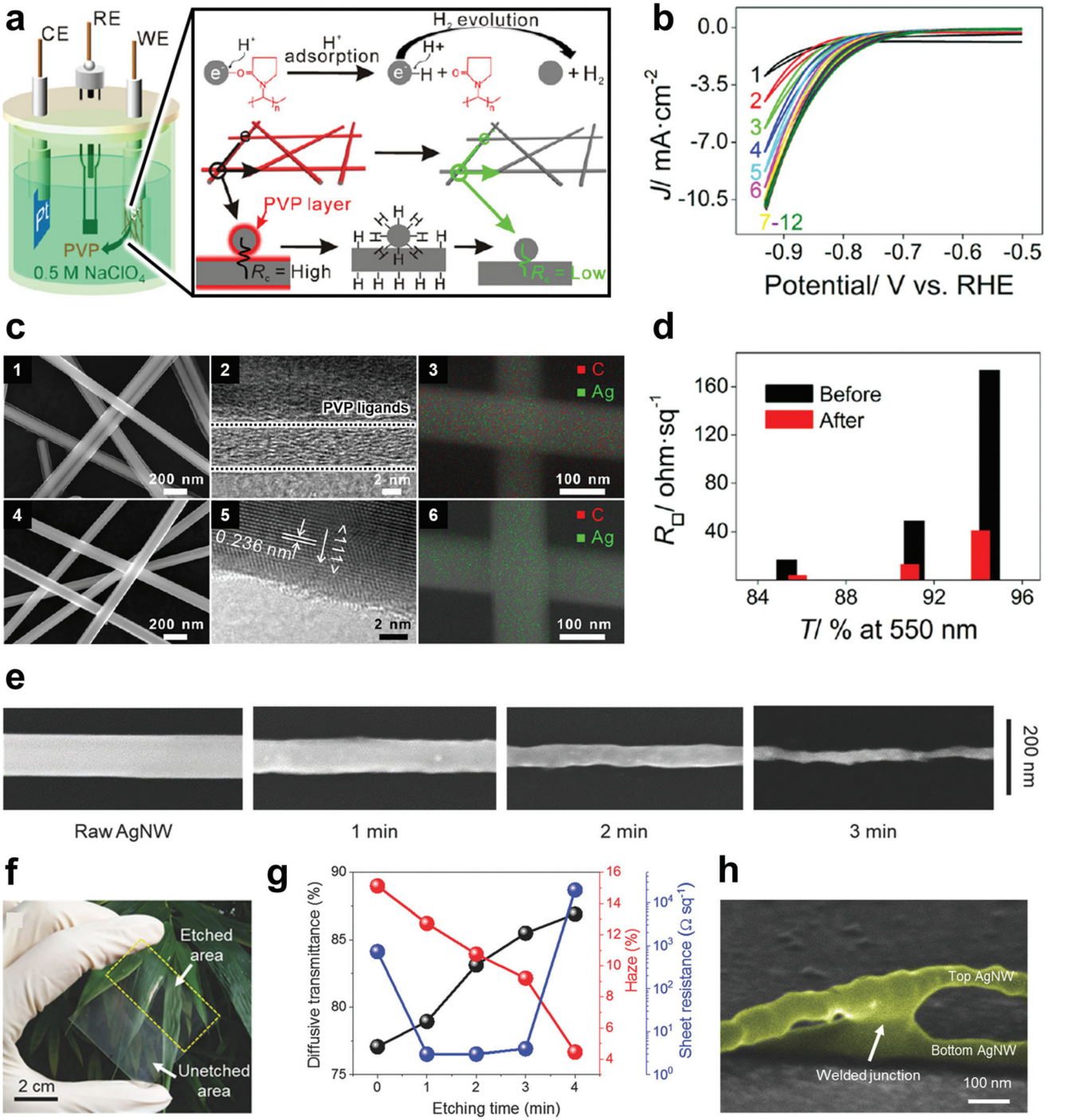

Fig. 2 (a) Schematic representation of the electrochemical cleaning of PVP ligands on the Ag NW surface using the HER. (b) CV curves over the narrow potential range involving the HER region as a function of the cycle number. (c) Scanning electron microscopy (SEM), high-resolution transmission electron microscopy (HR-TEM), and energy-dispersive X-ray spectroscopy (EDS) mapping images of Ag NWs before (1, 2, 3) and after (4, 5, 6) cleaning. (d) Sheet resistance and transmittance of Ag NW films before and after cleaning. Reproduced with permission.[87] Copyright 2019, American Chemical Society. (e) SEM images of Ag NWs with increasing electrochemical etching time. (f) Photographs of Ag NW films before and after etching. (g) Changes in diffusive transmittance and haze as a function of etching time. (h) Tilted side-view SEM image of electrochemically etched Ag NW films with welded junctions. Reproduced with permission.[93] Copyright 2018, Wiley-VCH.

neighboring ligand-free Ag NWs can spontaneously occur without additional thermal and/or mechanical treatments, which resulted in metallic fusion within Ag NW films even at room temperature (Fig. 2h).[75,94] As a result, the etched Ag NW films showed an extremely low sheet resistance of 4 Ω sq^{-1} with a high transmittance of 88.4% at a wavelength of 550 nm.

2.2 Chemical desorption-based interfacial control

The ligand desorption approach based on the use of chemical agents has been recognized as an effective interfacial control method, as reported by many research groups.[95–104] Chemical agents can induce the desorption of organic ligands by providing stronger affinities with the surface of metal and/or metal oxide nanomaterials than anchoring groups of ligands. For example, halide ions such as Br^- or Cl^- are well known to strongly detach organic ligands on the Ag surface and used for the preparation of highly conductive Ag NP (or NW) films.[95–97] Kagan and coworkers also reported that anionic thiocyanate ions can be chemisorbed onto positively charged sites on the Ag NP surface while removing organic ligands.[98] Additionally, Heo *et al.* reported that organic ligands adsorbed on the surface of metal oxide NPs, such as TCO NPs, can be completely stripped by nitrosonium tetrafluoroborate ($NOBF_4$) treatment.[100]

Ge *et al.* reported that $NaBH_4$ treatment can thoroughly remove the remaining PVP ligands within spin-coated Ag NW films, thereby providing direct welding between adjacent Ag NWs at room temperature.[57] During $NaBH_4$ treatment, hydride ions produced from $NaBH_4$ bound to the Ag NW surface (binding energy ~81.7 kJ mol^{-1}), rapidly displacing the carbonyl groups of PVP ligands (binding energy ~50.9 kJ mol^{-1}) (Fig. 3a). Consequently, the PVP ligands adsorbed on the Ag NW surface were clearly eliminated without impairing the overall structure and optical transparency of the Ag NW films even after $NaBH_4$ treatment (Fig. 3b and c). The chemically treated Ag NW films exhibited a low sheet resistance of 35 Ω sq^{-1} with a high transmittance of 92.6% at a wavelength of 550 nm (Fig. 3d). Additionally, it has been demonstrated that subsequent decoration with hydrophobic dodecanethiol (DT) layers onto the ligand-free Ag NW surface can effectively hinder moisture diffusion and/or surface oxidation, thus improving the long-term stability without affecting the optical/electrical properties of Ag NW films (Fig. 3e). Similarly, Zhu *et al.* prepared Ag NW-based TCEs using $NaBH_4$ treatment, followed by coating with poly(diallyldimethyl-ammonium chloride) (PDDA) layers onto Ag NW films to ensure long-term stability and surface planarization.[58] The resultant Ag NW/PDDA composite films showed uniform percolating networks after $NaBH_4$ treatment and PDDA coating (Fig. 3f). In particular, the root-mean-square (RMS) roughness of the Ag NW/PDDA composite films was decreased to ~13.5 nm with the aid of coating PDDA layers. Resultantly, the Ag NW/PDDA composite films showed a sheet resistance of 22 Ω sq^{-1} at a transmittance of 95.5% relative to the substrates (Fig. 3g) and markedly enhanced long-term stability compared to the pristine Ag NW films (Fig. 3h).

Crockett *et al.* prepared ITO NP-based TCEs using ligand desorption by formic acid treatment.[104] When the spin-coated ITO NP films were immersed in a formic acid/acetonitrile solution, the oleate ligands (*i.e.*, the conjugate base of OA) bound to the NP surface were protonated by formic acid, inducing the desorption of OA ligands and the simultaneous adsorption of formate ligands (*i.e.*, the conjugate base of formic acid) (Fig. 4a).[105] After the removal of OA ligands, the ITO NP films were thermally annealed at 300 °C under a reducing atmosphere to increase the oxygen vacancies within ITO NPs as well as to eliminate residual organic components. Scanning electron microscopy (SEM) images showed that the ITO NP films were uniformly deposited over the entire surface without any voids or cracks (Fig. 4b). In particular, the optical/electrical properties of ITO NP films depending on the size of NPs were systematically examined by comparing films consisting of NPs with diameters of 5.3, 12.8, and 21.5 nm (Fig. 4c). Three different ITO NP films with a similar thickness of ~150 nm showed a transmittance in the range of 85–88% at a wavelength of 550 nm, indicating that the size of ITO NPs did not have a significant impact on optical transparency (Fig. 4d). On the other hand, the sheet resistance of ITO NP films decreased over an order of magnitude from 3690 to 350 Ω sq^{-1} for 5.3 and 21.5 nm NPs, respectively (Fig. 4e). This trend in the electrical properties was explained by the decreases in coulombic charging energy and interface density as the size of ITO NPs increased, resulting in the lowered activation energy for hopping conduction at the NP–NP interfaces (Fig. 4f). That is, these phenomena strongly suggest that the degree of the existing interfaces with organic ligands has a decisive effect on the electrical conduction within nanocomposite electrodes.[50]

2.3 Electrostatic LbL assembly-based interfacial control

Among the various solution approaches, LbL assembly based on complementary interactions (mainly electrostatic interactions) between components offers diverse opportunities to prepare nanocomposite films with tailored thicknesses, compositions, and functionalities on various substrates irrespective of substrate size and shape.[106–112] In line with these notable advantages, a variety of charged conductive materials (*e.g.*, charged metal NPs/NWs, CNTs, r-GOs, and conducting polymers) in aqueous media have been electrostatically LbL-assembled with oppositely charged materials for the preparation of TCEs.[113–119] For example, Hong *et al.* reported that when positively charged CNTs (NH_3^+-CNTs) were LbL-assembled with negatively charged r-GOs (COO^--r-GOs), the formed multilayers exhibited a sheet resistance of 8 kΩ sq^{-1} with a transmittance of 81.0% at a wavelength of 550 nm.[116] Recently, Camic *et al.* demonstrated that the relatively high sheet resistance of electrostatically LbL-assembled films can be lowered by the use of Ag NWs instead of CNTs.[117] For this study, positively charged Ag NWs (NH_3^+-Ag NWs) were first prepared by ligand exchange between cysteamine and PVP ligands on the surface of Ag NWs. These cationic NH_3^+-Ag NWs were LbL-assembled with anionic GOs for the preparation of (anionic GO/NH_3^+-Ag NWs)$_n$ multilayers (herein, 'n' is the bilayer number) onto glass substrates. The total resistance of (anionic GO/NH_3^+-Ag NWs)$_n$ multilayers was significantly decreased because cysteamine is a small molecule with an extremely low M_w of ~77 g mol^{-1}; additionally, the LbL-assembled GOs were

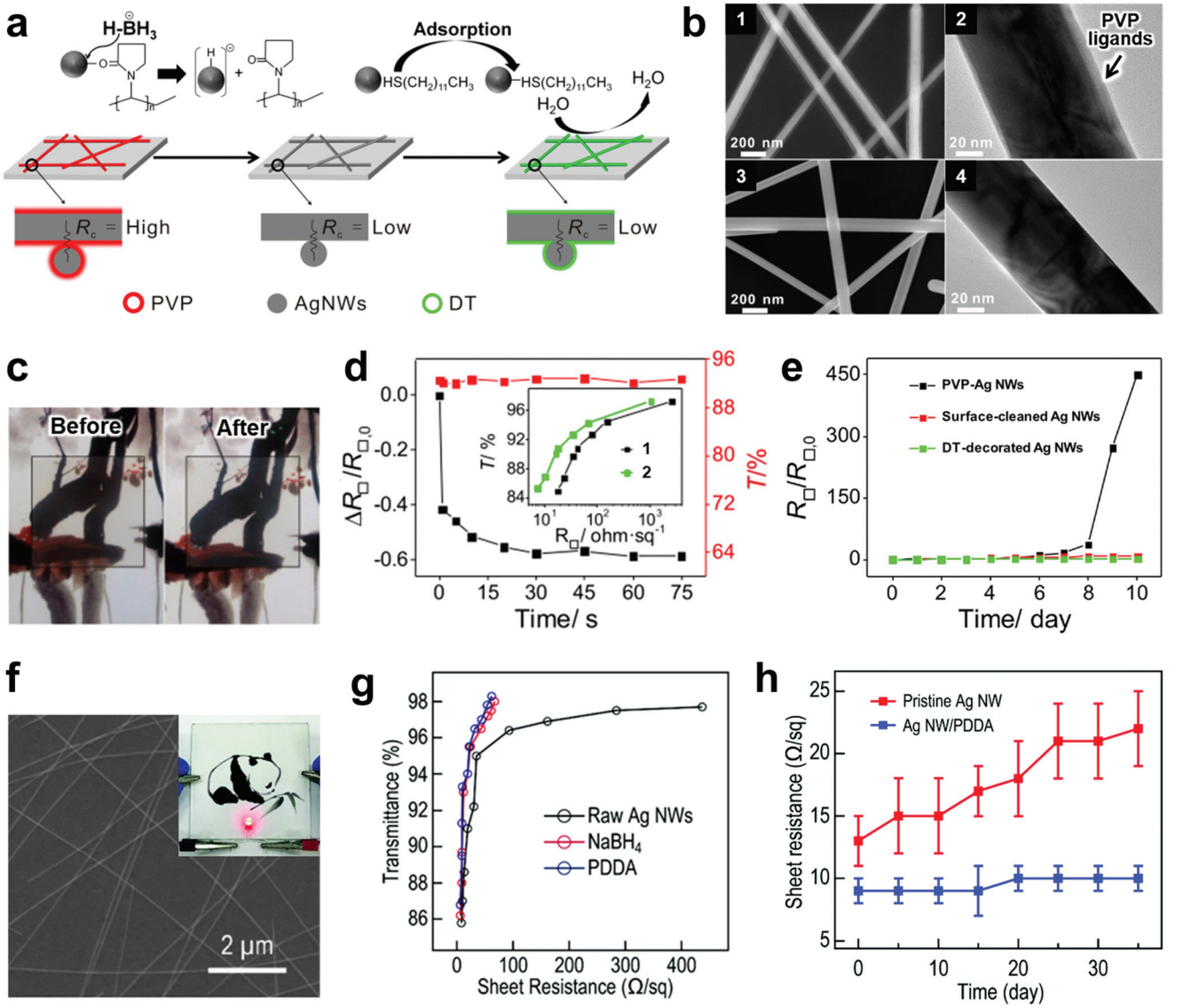

Fig. 3 (a) Schematic representation of the removal of PVP ligands from Ag NWs through chemical desorption using $NaBH_4$ treatment and subsequent surface decoration of DT layers. (b) SEM and HR-TEM images of Ag NWs before (1, 2) and after (3, 4) $NaBH_4$ treatment. (c) Photographs of Ag NW films before and after $NaBH_4$ treatment. (d) Changes in the relative sheet resistance and transmittance of Ag NW films with increasing $NaBH_4$ treatment time. The inset shows the plot of transmittance *versus* sheet resistance of Ag NW films before (black line, 1) and after (green line, 2) $NaBH_4$ treatment. (e) Variations in sheet resistance for PVP-Ag NW, surface-cleaned Ag NW, and DT-decorated Ag NW films exposed in summer air (temperature ~25 °C; relative humidity ~90%) for 10 days. Reproduced with permission.[57] Copyright 2018, American Chemical Society. (f) Planar SEM and photograph of Ag NW/PDDA composite films. (g) Plots of transmittance *versus* sheet resistance of Ag NW films according to $NaBH_4$ treatment and PDDA coating. (h) Stability tests of PVP-Ag NW and Ag NW/PDDA composite films under 25 °C/65% relative humidity conditions. Reproduced with permission.[58] Copyright 2020, The Royal Society of Chemistry.

transformed into r-GOs through chemical reduction using hydrazine treatment. When the (anionic r-GO/NH_3^+-Ag NWs)$_2$ multilayers were thermally annealed at 230 °C, the resultant multilayers exhibited a low sheet resistance of 6.5 Ω sq^{-1} with a transmittance of 78.2%.

On the other hand, when using metal NPs with a high degree of light reflection as conductive nanomaterials for TCEs, the total thickness of the assembled films should be controlled below ~10 nm for visible light transmission.[18,120] Furthermore, the packing density of these NPs in the lateral dimension should be also substantially increased to decrease the contact resistance (*i.e.*, the separation distance due to a low packing density and the presence of organic ligands) occurring between adjacent metal NPs.[76] However, when charged metal NPs are LbL-assembled with oppositely charged polymer linkers, the packing density of metal NPs per layer is generally below ~30%, which is mainly caused by electrostatic repulsion between the same charged metal NPs.[121] Therefore, electrostatically LbL-assembled metal NP films with a low thickness (<10 nm) have poor electrical conductivity that is

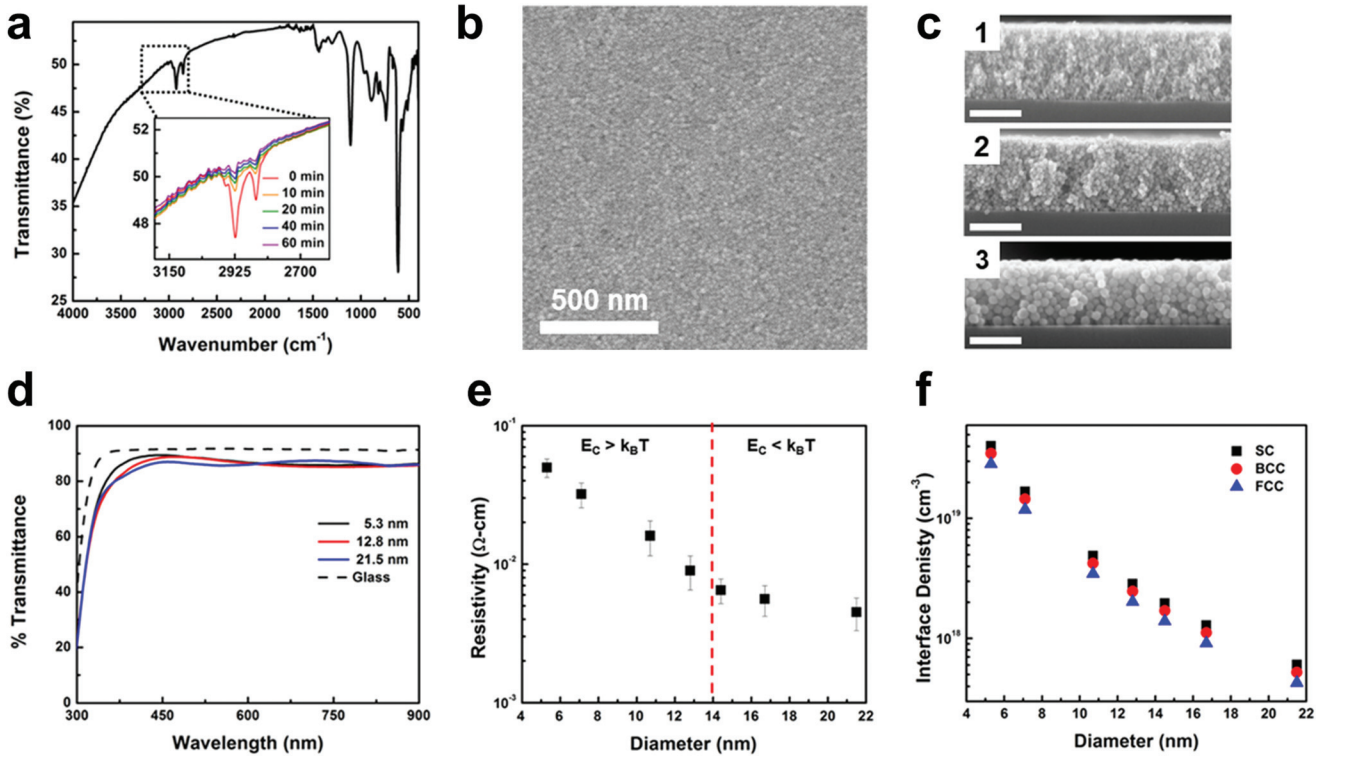

Fig. 4 (a) Fourier transform infrared (FTIR) spectra of ITO NP films during ligand exchange reactions. The C–H stretching peaks related to oleate ligands decrease as the substitution with formate ligands progresses. (b) Planar SEM image of ITO NP films after ligand exchange reactions. (c) Cross-sectional SEM images of ITO NP films composed of NPs with diameters of 5.3 nm (1), 12.8 nm (2), and 21.5 nm (3). (d) Optical transmittance spectra of ITO NP films with different NP sizes. (e) Changes in the resistivity of ITO NP films with a thickness of ~150 nm as a function of NP diameter. When the ITO NP diameter is larger than 14 nm, the coulombic charging energy (E_c) becomes lower than the thermal energy (k_BT), dividing into two separate regions with different size dependencies for the activation energy. (f) Evaluated interface densities of ITO NP films depending on the NP diameter using the sphere packing geometries of simple cubic (SC), body-centered cubic (BCC), and face-centered cubic (FCC). Reproduced with permission.[104] Copyright 2019, American Chemical Society.

close to an insulating property because of the low degree of interconnection among neighboring NPs.[76] Additionally, the polymer linkers mainly used for electrostatic LbL assembly increase the contact resistance within the assembled metal NP films,[110] which is similar to the case with bulky/insulating organic ligands. These phenomena imply that even if electrostatically LbL-assembled TCO NP films with minimal light reflectance/absorption can be applied to TCEs, their low electrical conductivity originating from both the low packing density of TCO NPs (by electrostatic repulsion) and the presence of bulky polymer linkers remains an unavoidable drawback.[122] Therefore, a more advanced solution approach allowing the use of a wide range of conductive nanomaterials is required for developing high-performance TCEs with the desired functionalities.

2.4 LR-LbL assembly-based interfacial control

Recently, it was demonstrated that organic linkers with NH_2 and COOH groups, which serve as bidentate or multidentate ligands, can directly bridge the interfaces between adjacent inorganic NPs (*i.e.*, metal and/or metal oxide NPs) by effectively replacing bulky organic ligands on the surface of NPs during LbL assembly in organic media.[70–77] These ligand replacement reactions are mainly caused by the higher affinity of multidentate linkers with the NP surface than that of monodentate organic ligands.[70] Specifically, NH_2- or COOH-functionalized small molecular linkers such as tris(2-aminoethyl)amine (TREN, $M_w \sim 146$), diethylenetriamine (DETA, $M_w \sim 104$), hydrazine (Hyd, $M_w \sim 32$), and tricarballylic acid (TC, $M_w \sim 176$) in ethanol can be LbL-assembled by successfully substituting hydrophobic organic ligands (*e.g.*, OA, OAm, and TOA) on the surface of metal (*e.g.*, Au, Ag, Cu, and Pt) and/or metal oxide (*e.g.*, ITO, FeO_x, MnO_x, WO_x, and TiO_x) NPs in nonpolar media.[60,72,75,123–125] This LR-LbL assembly using small molecular linkers in organic media without electrostatic repulsion can lead to the formation of densely packed NP films and significantly decrease the interparticle distance between adjacent NPs.[59] In this case, the separation distance of metal NP–NP at the interfaces was estimated to be less than 6 Å by atomistic molecular dynamic (MD) simulations, suggesting the possibility of greatly enhanced charge transport between neighboring NPs.[75,77]

Based on the notable advantages of LR-LbL assembly, Cho *et al.* reported that OAm-ITO NPs can be LbL-assembled with small Hyd molecules composed of only two NH_2 groups (Fig. 5a).[123] It has also been demonstrated that the use of

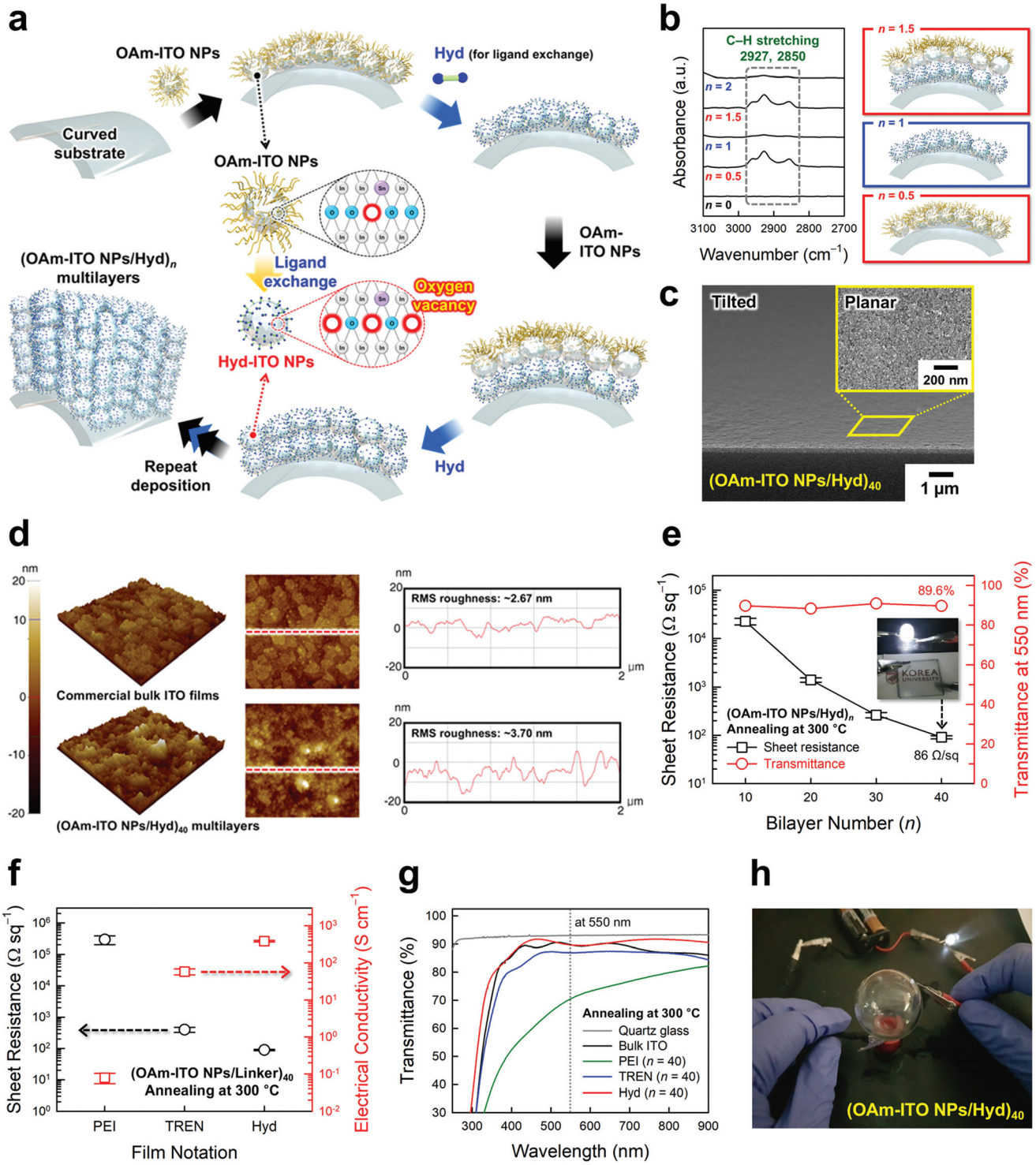

Fig. 5 (a) Schematic illustration of the preparation of ITO NP multilayers on curved substrates based on LR-LbL assembly using small Hyd linkers with carbon-free and chemically reducing properties. (b) FTIR spectra and schematic representation of (OAm-ITO NPs/Hyd)$_n$ multilayers as a function of bilayer number (n). The disappearance and regeneration of C–H stretching peaks indicate ligand exchange reactions between OAm ligands and Hyd linkers. (c) Tilted and planar (inset) SEM images of (OAm-ITO NPs/Hyd)$_{40}$ multilayers. (d) Atomic force microscopy (AFM) images and height profiles of commercial bulk ITO films and (OAm-ITO NPs/Hyd)$_{40}$ multilayers. (e) Sheet resistance, transmittance, and photographic image (inset) of (OAm-ITO NPs/Hyd)$_n$ multilayers after thermal annealing at 300 °C as a function of the bilayer number. (f) Electrical and (g) optical properties of ITO NP multilayers based on three different NH_2-functionalized linkers (PEI, TREN, and Hyd) after thermal annealing at 300 °C. (h) Photograph of the (OAm-ITO NPs/Hyd) multilayer-coated spherical glass connected with an LED. Reproduced with permission.[123] Copyright 2020, Wiley-VCH.

carbon-free Hyd linkers with strong chemically reducing properties can increase the oxygen vacancies within ITO NPs during LbL assembly, which has a significant effect on the electrical conductivity of ITO NP films. The Hyd linkers were adsorbed on the surface of ITO NPs through a consecutive ligand replacement reaction between the NH_2 groups of Hyd linkers and the OAm ligands (Fig. 5b). The LR-LbL-assembled $(OAm\text{-}ITO\ NPs/Hyd)_{40}$ multilayers showed a densely packed surface morphology with a low RMS roughness of ~3.70 nm (Fig. 5c and d). When the formed $(OAm\text{-}ITO\ NPs/Hyd)_{40}$ multilayers were annealed at 300 °C under an Ar/H_2 gas mixture to increase the ratio of oxygen vacancies within ITO NPs, the sheet resistance was evaluated to be 86 Ω sq^{-1}, while the initial transmittance of ~89.6% at a wavelength of 550 nm was maintained (Fig. 5e). Particularly, when increasing the annealing temperature up to 400 °C, the sheet resistance of $(OAm\text{-}ITO\ NPs/Hyd)_{40}$ multilayers was decreased up to 30 Ω sq^{-1}. As already mentioned, this excellent electrical/optical performance of $(OAm\text{-}ITO\ NPs/Hyd)_n$ multilayers was mainly attributed to the use of extremely small Hyd linkers ($M_w \sim 32$) with carbon-free and reducing properties, which could be more clarified by comparison with two different NH_2-functionalized linkers (*i.e.*, poly(ethylene imine) (PEI, $M_w \sim 800$) and TREN ($M_w \sim 146$)). The sheet resistances of PEI and TREN linker-based ITO NP films were found to be $\sim 2.3 \times 10^5$ and ~346 Ω sq^{-1}, respectively (Fig. 5f). Furthermore, these PEI and TREN linker-based ITO NP films exhibited a notable decrease in transmittance after annealing processes due to the light absorption of the formed carbon residues, which was in stark contrast to Hyd linker-based films (Fig. 5g). Additionally, the Hyd linker-based ITO NP films had a higher ratio of oxygen vacancies (~59%) than those of PEI (~33%) and TREN (~42%) linker-based films under the same annealing conditions. These results imply that the physical and/or chemical properties of linkers can directly affect the electrical conductivity as well as the optical transparency of ITO NP-based TCEs. Moreover, the LR-LbL assembly of ITO NPs based on the dipping process could be easily applied to highly curved substrates such as spherical glasses (Fig. 5h).

3. Electrochemical applications using interface-controlled TCO NPs

3.1 Transparent supercapacitors

Pseudocapacitive (PC)-TMO NPs, which provide a high energy storage performance through faradaic redox reactions at or near the surface of NPs, have been extensively used as active materials for energy storage devices such as supercapacitors.[126–130] However, for PC-TMO NP-based electrodes to be applied to transparent supercapacitors (TSCs), they should have a limited film thickness due to the inherent opacity and poor electrical conductivity of TMO NPs.[126] Therefore, it remains a great challenge to overcome the complex trade-off between capacitance (particularly areal capacitance (C_{areal})) and optical transparency as well as to enhance the rate capability of PC-TMO NP-based electrodes.[127]

Transparent/conductive ITO NPs can also possess charge-storage capability through electrical double-layer capacitor (EDLC) behaviors, which originate from their large surface-to-volume ratio.[131,132] Bellani *et al.* prepared ITO NP-based electrodes by drop-casting cubic-shaped ITO NPs with a lateral dimension of less than 50 nm (Fig. 6a).[131] The specific surface area of the nanostructured ITO NP films was 249 times larger than that of bulk ITO films at a loading amount of 1 mg cm^{-2} (Fig. 6b and c), as measured by Brunauer–Emmett–Teller (BET) analysis. The ITO NP-based electrodes showed nearly rectangular CV curves of EDLC behaviors without obvious redox peaks, maintaining their shapes even at a high scan rate of up to 10 V s^{-1} (Fig. 6d and e). These ITO NP-based electrodes exhibited a C_{areal} value of 1.53 mF cm^{-2} (@ 0.2 mA cm^{-2}) with a transmittance of 64.4% (@ 550 nm; Fig. 6f) at a loading amount of 0.50 mg cm^{-2}, whereas bulk ITO electrodes had a negligible capacitance.

Cho *et al.* further demonstrated that interface-controlled ITO NP films using smaller NPs (~8 nm; Fig. 7a) with a more uniform size can exhibit improved optical/electrochemical properties.[123] Specifically, the LR-LbL assembly of OAm-ITO NPs and small Hyd linkers produced nanocomposite films with high optical transparency (by the formation of a smooth surface morphology) and a large active area (Fig. 7b). As a result, the LR-LbL-assembled $(OAm\text{-}ITO\ NPs/Hyd)_n$ multilayers showed almost quasi-rectangular CV shapes with typical EDLC behaviors and fast current responses (Fig. 7c). Due to the well-defined ITO NPs and the LR-LbL assembly modulating facile charge transport, the C_{areal} and transmittance values of $(OAm\text{-}ITO\ NP/Hyd)_{40}$ multilayers (the loading amount of ITO NPs was ~0.16 mg cm^{-2}) were evaluated to be approximately 1.44 mF cm^{-2} (@ 0.2 mA cm^{-2}) and 89.6% (@ 550 nm), respectively. This electrochemical performance of ITO NP-based electrodes can be further enhanced by the integration of PC-MnO NPs within the assembled films. Choi *et al.* reported that high-performance TSC electrodes with high C_{areal} values can be prepared by alternating the LR-LbL assembly of OA-MnO NPs and OAm-ITO NPs with small TC linkers (Fig. 7d).[124] The bulky/insulating organic ligands (*i.e.*, OA and OAm) loosely bound to the surfaces of MnO and ITO NPs were successfully replaced by multidentate TC linkers with three COOH groups.[105,133] Additionally, the use of TC linkers induced the homogeneous insertion of ITO NPs without agglomerations into the densely packed NP arrays, which contributed to the formation of an efficient charge pathway across electrodes (Fig. 7e). Therefore, the charge-storage capability of the $(MnO\ NP/TC/ITO\ NP/TC)_m$ multilayers (herein, '*m*' is the periodic number) was notably improved compared to that of the $(ITO\ NP/TC)_n$ and $(MnO\ NP/TC)_n$ multilayers, as shown in the CV curves (Fig. 7f). In particular, given that the electrical double-layer capacitance of ITO NPs was much lower than the pseudocapacitance of

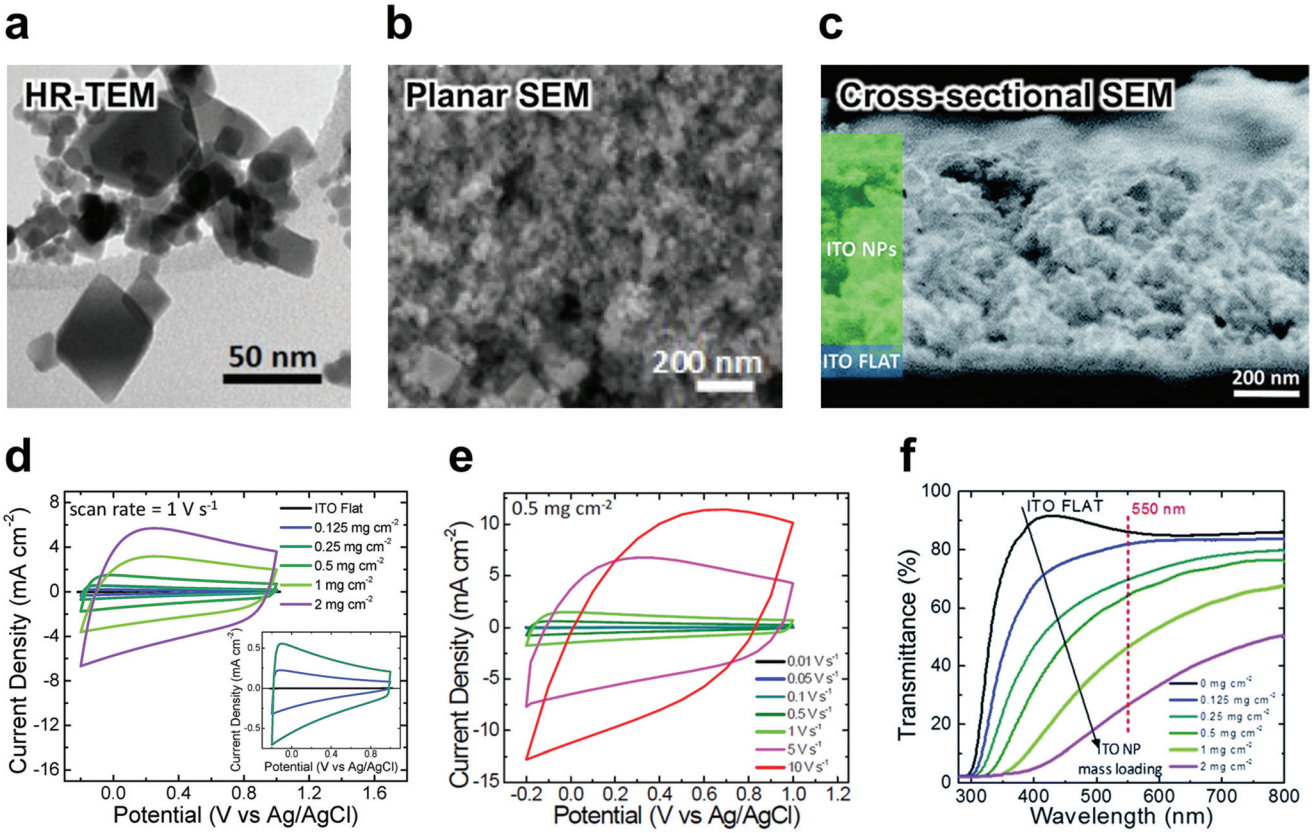

Fig. 6 (a) HR-TEM image of ITO NPs with lateral dimensions of less than ~50 nm. (b) Planar and (c) cross-sectional SEM images of drop-casted ITO NP films at a loading amount of 1 mg cm^{-2}. (d) CV curves of ITO NP films at a scan rate of 1 V s^{-1} with an increasing loading amount from 0 to 2 mg cm^{-2}. (e) CV curves of ITO NP films at a loading amount of 0.50 mg cm^{-2} at different scan rates (from 0.01 to 10 V s^{-1}). (f) Optical transmittance spectra of ITO NP films with an increasing loading amount from 0 to 2 mg cm^{-2}. Reproduced with permission.[131] Copyright 2017, The Royal Society of Chemistry.

MnO NPs, the prominent enhancement was mainly attributed to the reduced internal resistance by inserting ITO NPs. Electrochemical impedance spectroscopy (EIS) analysis also confirmed that ITO NP-incorporated MnO NP-based electrodes exhibited lower equivalent series resistance and charge transfer resistance than ITO NP-free electrodes (Fig. 7g). As a result, the C_{areal} value of $(MnO\ NP/TC/ITO\ NP/TC)_{50}$ multilayers was substantially increased from 24.6 to 40.5 mF cm^{-2} (@ 0.1 mA cm^{-2}) with the insertion of ITO NPs; on the other hand, the optical transmittance was slightly decreased from 61.6% to 60.8% (@ 550 nm), which also outperformed the electrochemical performance of $(ITO\ NP/TC)_{50}$ and $(MnO\ NP/TC)_{50}$ multilayers (Fig. 7h).

3.2 EC devices

EC-TMOs, which can allow reversible electrochemical reaction-induced color switching by external electrical potentials, have attracted considerable attention due to their potential uses for a variety of applications, such as automotive displays and energy-saving smart windows.[134–137] However, similar to the case with PC-TMO NPs for TSC electrodes, EC-TMOs also suffer from sluggish charge transfer kinetics due to their poor electrical conductivity.[136] Although solution-processable EC-TMO nanomaterials prepared in organic media can have some advantages in improving their charge transport within electrodes, it should be noted that bulky/insulating organic ligands bound to the surface of EC-TMO nanomaterials act as another obstacle to charge delivery between neighboring EC-TMO nanomaterials.[62] Additionally, considering that reversible color changes of EC-TMO nanomaterials are closely related to the insertion/extraction of guest positive ions (*e.g.*, Li^+, H^+, and Na^+) and electrons, their switching behaviors for coloration and/or bleaching are greatly influenced by the degree of charge transfer.[137] Therefore, as mentioned earlier, uniform incorporation of interface-controlled TCO NPs into EC-TMO nanocomposite films can enhance the overall EC performance without sacrificing the optical transparency of electrodes.

Recently, Yun *et al.* reported that LR-LbL-assembled nanocomposite films composed of OAm-$WO_{2.72}$ NRs, OAm-ITO NPs, and TREN linkers can exhibit a high EC performance (*i.e.*, a fast color switching speed and a high color contrast) due to the improved charge transfer by the aid of conductive ITO NPs, small TREN linkers, and NR-induced porous struc-

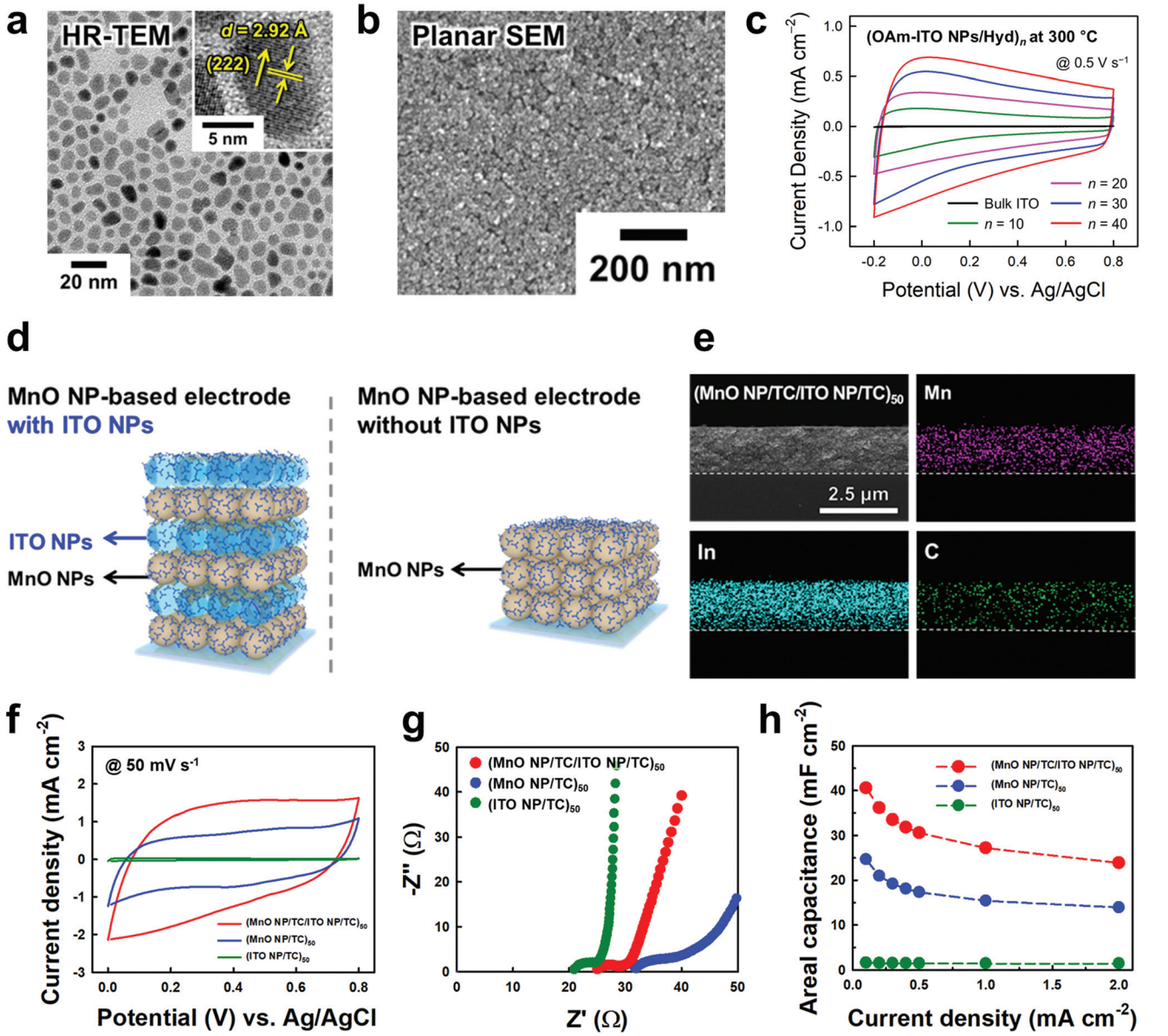

Fig. 7 (a) HR-TEM image of ITO NPs with a diameter of ~8 nm. (b) Planar SEM image of LR-LbL-assembled (OAm-ITO NPs/Hyd) multilayers. (c) CV curves of (OAm-ITO NPs/Hyd) multilayers a scan rate of 0.5 V s^{-1} with an increasing bilayer number (*n*) from 0 to 40. Reproduced with permission.[123] Copyright 2020, Wiley-VCH. (d) Schematic representation of MnO NP-based electrodes with the incorporation of ITO NPs prepared by LR-LbL assembly using small TC linkers. (e) EDS mapping images of $(MnO\ NP/TC/ITO\ NP/TC)_{50}$ multilayers. Comparison of (f) CV curves at a scan rate of 50 mV s^{-1}, (g) Nyquist plots, and (h) areal capacitance among $(MnO\ NP/TC/ITO\ NP/TC)_{50}$, $(MnO\ NP/TC)_{50}$, and $(ITO\ NP/TC)_{50}$ multilayers. Reproduced with permission.[124] Copyright 2019, American Chemical Society.

tures (Fig. 8a).[125] During consecutive LR-LbL assembly, OAm-$WO_{2.72}$ NRs were vertically bridged with small TREN linkers, generating a number of nanosized pores formed among the randomly packed $WO_{2.72}$ NRs (Fig. 8b).[63] In this case, OAm-ITO NPs with a diameter of ~7 nm could easily infiltrate into the $WO_{2.72}$ NR films through the nanosized pores (Fig. 8b and c). Although the inserted ITO NPs had little effect on the optical transparency of $WO_{2.72}$ NR-based electrodes in the bleached state, the ITO NP-incorporated $WO_{2.72}$ NR-based electrodes showed improved optical modulations (*i.e.*, transmittance changes between bleached and colored states at a wavelength of 633 nm) compared to the ITO NP-free electrodes (Fig. 8d). Furthermore, the switching times of $WO_{2.72}$ NR-based electrodes for coloration/bleaching notably decreased from 12.2 s/6.5 s to 5.0 s/3.0 s (m = 20) and 44.2 s/53.2 s to 10.9 s/15.2 s (m = 40) due to the enhanced charge transport by the insertion of ITO NPs (Fig. 8e and f). These phenomena were also confirmed by the decreased charge transfer resistance and ion diffusion resistance of ITO NP-incorporated $WO_{2.72}$ NR-based electrodes, as shown in EIS

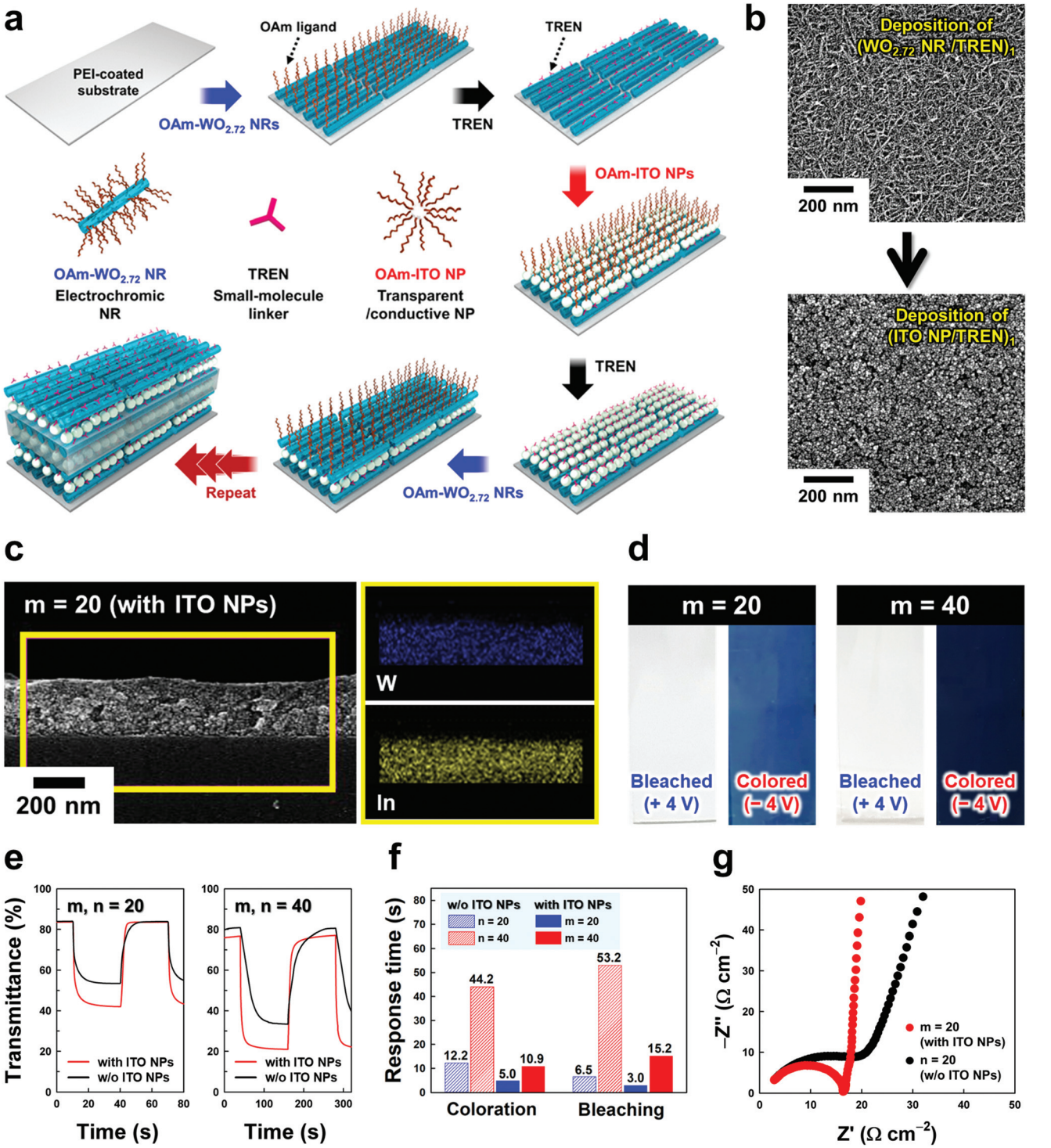

Fig. 8 (a) Schematic illustration of the alternating LR-LbL assembly of OAm-$WO_{2.72}$ NRs and OAm-ITO NPs using small TREN linkers. (b) Surface morphology according to the sequential deposition of ($WO_{2.72}$ NR/TREN) and (ITO NP/TREN) layers. (c) Cross-sectional SEM and EDS mapping images of ($WO_{2.72}$ NR/TREN/ITO NP/TREN)$_{20}$ multilayers. (d) Photographs of ($WO_{2.72}$ NR/TREN/ITO NP/TREN)$_{20\ and\ 40}$ multilayers in bleached (+4.0 V) and colored (−4.0 V) states. Comparison of (e) switching behaviors, (f) response times for coloration/bleaching, and (g) Nyquist plots of $WO_{2.72}$ NR-based electrodes with ITO NPs and without ITO NPs. Reproduced with permission.[125] Copyright 2019, The Royal Society of Chemistry.

analysis (Fig. 8g). Particularly, considering that the periodic incorporation of ITO NPs into $WO_{2.72}$ NR-based electrodes increased the total film thickness and partially fills the nanopores, a notable increase in the EC performance was primarily due to the enhanced charge transport by inserting ITO NPs.

4. Conclusions and outlook

Interfacial control on solution-processable nanomaterials (particularly metal and/or metal oxide nanomaterials) plays a critical role in determining the electrical and/or electrochemical performance of transparent nanocomposite electrodes. However, although this control is an important issue, most solution approaches reported to date have been recognized as only one tool for coating high-quality nanomaterials (*i.e.*, in terms of high dispersion stability, high crystallinity, and uniform size/shape) onto transparent substrates without careful consideration of ligand control and the interfacial interactions of electrically and/or electrochemically active nanomaterials. Particularly, when preparing TCEs based on solution-processable conductive nanomaterials, bulky/insulating organic ligands inevitably cause high contact resistance at the interfaces, which seriously restricts charge transfer across the assembled TCEs. Furthermore, in the case of TCO NP-based TCEs, the carbon residues generated from thermal decomposition of hydrocarbon-based ligands during annealing processes at high temperatures notably decrease the optical transparency of TCEs due to their strong light absorption.

From this viewpoint, we have discussed the need for interfacial control and optimal solution approaches to prepare TCEs with desirable optical/electrical performance. Among the various interfacial control approaches, LR-LbL assembly using small molecular linkers in organic media could significantly enhance the electrical conductivity of TCO NP-based TCEs due to the minimized interparticle distance between neighboring NPs as well as the increase in oxygen vacancies by the reducing properties of the NH_2-functionalized linkers. Additionally, even if the TCO NP-based TCEs need annealing processes at high temperatures to further enhance their electrical performance, the effect of the formed carbon residues (by partially decomposed organic ligands and/or linkers) on the optical transparency could be minimized through the use of extremely small and/or carbon-free linkers. Owing to the facile control and design of the interfacial structure using LR-LbL assembly, TCO NPs could be uniformly nanoblended with other kinds of TMO NPs or NRs, which can allow the preparation of transparent nanocomposite electrodes with the desired functionalities. In this case, the unfavorable trade-off between electrical and/or electrochemical performance and optical transparency for transparent nanocomposite electrodes (*i.e.*, TCEs, TSC electrodes, and EC electrodes) could be mitigated to some degree using interface-controlled TCO NPs by LR-LbL assembly.

However, despite these notable advantages of LR-LbL assembly, thin-film deposition through repetitive coating processes brings about time-consuming issues. Although an increase in solution concentration can significantly reduce the adsorption time and increase the packing density (*i.e.*, the loading amount) of NPs,[70] it is highly desirable that more universal and commercial approaches, such as roll-to-roll or spray-coating methods, are combined with LR-LbL assembly for process efficiency.[138,139] We believe that these efforts to combine approaches can represent a technological breakthrough for the practical production of high-performance transparent nanocomposite electrodes using interfacial control and interactions; furthermore, these combinatorial approaches or modified LbL assembly approaches can be widely and effectively applied to various electrical and/or electrochemical applications.

Conflicts of interest

There are no conflicts to declare.

Acknowledgements

This work was supported by the National Research Foundation of Korea (NRF) grant funded by the Korea government (MSIT; Ministry of Science and ICT) (No. 2019R1A4A1027627, 2018R1A2A1A05019452, and 2016M3A7B4910619).

References

1 D. S. Ginley and C. Bright, *MRS Bull.*, 2000, **25**, 15–18.
2 K. Ellmer, *Nat. Photonics*, 2012, **6**, 809–817.
3 H. Wu, D. Kong, Z. Ruan, P.-C. Hsu, S. Wang, Z. Yu, T. J. Carney, L. Hu, S. Fan and Y. Cui, *Nat. Nanotechnol.*, 2013, **8**, 421–425.
4 J. Liang, L. Li, X. Niu, Z. Yu and Q. Pei, *Nat. Photonics*, 2013, **7**, 817–824.
5 Y. Sun, M. Chang, L. Meng, X. Wan, H. Gao, Y. Zhang, K. Zhao, Z. Sun, C. Li, S. Liu, H. Wang, J. Liang and Y. Chen, *Nat. Electron.*, 2019, **2**, 513–520.
6 Y. Zhang, S.-W. Ng, X. Lu and Z. Zheng, *Chem. Rev.*, 2020, **120**, 2049–2122.
7 S. Bae, H. Kim, Y. Lee, X. Xu, J.-S. Park, Y. Zheng, J. Balakrishnan, T. Lei, H. R. Kim, Y. I. Song, Y.-J. Kim, K. S. Kim, B. Özyilmaz, J.-H. Ahn, B. H. Hong and S. Iijima, *Nat. Nanotechnol.*, 2010, **5**, 574–578.
8 Y.-H. Liu, J.-L. Xu, X. Gao, Y.-L. Sun, J.-J. Lv, S. Shen, L.-S. Chen and S.-D. Wang, *Energy Environ. Sci.*, 2017, **10**, 2534–2543.
9 G. Cai, P. Darmawan, M. Cui, J. Wang, J. Chen, S. Magdassi and P. S. Lee, *Adv. Energy Mater.*, 2016, **6**, 1501882.
10 S. Lin, X. Bai, H. Wang, H. Wang, J. Song, K. Huang, C. Wang, N. Wang, B. Li, M. Lei and H. Wu, *Adv. Mater.*, 2017, **29**, 1703238.
11 R. M. Pasquarelli, D. S. Ginley and R. O'Hayre, *Chem. Soc. Rev.*, 2011, **40**, 5406–5441.
12 Z. Kan, Z. Wang, Y. Firdaus, M. Babics, H. N. Alshareef and P. M. Beaujuge, *J. Mater. Chem. A*, 2018, **6**, 10176–10183.
13 S. C. Dixon, D. O. Scanlon, C. J. Carmalt and I. P. Parkin, *J. Mater. Chem. C*, 2016, **4**, 6946–6961.
14 E. N. Dattoli and W. Lu, *MRS Bull.*, 2011, **36**, 782–788.

15 D. Li, W.-Y. Lai, Y.-Z. Zhang and W. Huang, *Adv. Mater.*, 2018, **30**, 1704738.
16 J. Song and H. Zeng, *Angew. Chem., Int. Ed.*, 2015, **54**, 9760–9774.
17 M. Layani, A. Kamyshny and S. Magdassi, *Nanoscale*, 2014, **6**, 5581–5591.
18 S. Ye, A. R. Rathmell, Z. Chen, I. E. Stewart and B. J. Wiley, *Adv. Mater.*, 2014, **26**, 6670–6687.
19 N. Zhou, D. B. Buchholz, G. Zhu, X. Yu, H. Lin, A. Facchetti, T. J. Marks and R. P. H. Chang, *Adv. Mater.*, 2014, **26**, 1098–1104.
20 D.-K. Hwang, M. Misra, Y.-E. Lee, S.-D. Baek, J.-M. Myoung and T. I. Lee, *Appl. Surf. Sci.*, 2017, **405**, 344–349.
21 N.-R. Kim, J.-H. Lee, Y.-Y. Lee, D.-H. Nam, H.-W. Yeon, S.-Y. Lee, T.-Y. Yang, Y.-J. Lee, A. Chu, K. T. Nam and Y.-C. Joo, *J. Mater. Chem. C*, 2013, **1**, 5953–5959.
22 X. Li, W. Cai, J. An, S. Kim, J. Nah, D. Yang, R. Piner, A. Velamakanni, I. Jung, E. Tutuc, S. K. Banerjee, L. Colombo and R. S. Ruoff, *Science*, 2009, **324**, 1312–1314.
23 Z. Yin, S. Sun, T. Salim, S. Wu, X. Huang, Q. He, Y. M. Lam and H. Zhang, *ACS Nano*, 2010, **4**, 5263–5268.
24 H. B. Lee, W.-Y. Jin, M. M. Ovhal, N. Kumar and J.-W. Kang, *J. Mater. Chem. C*, 2019, **7**, 1087–1110.
25 L. Li, B. Zhang, B. Zou, R. Xie, T. Zhang, S. Li, B. Zheng, J. Wu, J. Weng, W. Zhang, W. Huang and F. Huo, *ACS Appl. Mater. Interfaces*, 2017, **9**, 39110–39115.
26 T. Gao, B. Wang, B. Ding, J.-K. Lee and P. W. Leu, *Nano Lett.*, 2014, **14**, 2105–2110.
27 T. Qiu, B. Luo, E. M. Akinoglu, J.-H. Yun, I. R. Gentle and L. Wang, *Adv. Funct. Mater.*, 2020, **30**, 2002556.
28 C. F. Guo, T. Sun, Q. Liu, Z. Suo and Z. Ren, *Nat. Commun.*, 2014, **5**, 3121.
29 T. O. L. Sunde, E. Garskaite, B. Otter, H. E. Fossheim, R. Saeterli, R. Holmestad, M.-A. Einarsrud and T. Grande, *J. Mater. Chem.*, 2012, **22**, 15740–15749.
30 L. Kőrösi, A. Scarpellini, P. Petrik, S. Papp and I. Dékány, *Appl. Surf. Sci.*, 2014, **320**, 725–731.
31 Y. Liu, T. Moser, C. Andres, L. Gorjan, A. Remhof, F. Clemens, T. Graule, A. N. Tiwari and Y. E. Romanyuk, *J. Mater. Chem. A*, 2019, **7**, 3083–3089.
32 S.-G. Ban, K.-T. Kim, B. D. Choi, J.-W. Jo, Y.-H. Kim, A. Facchetti, M.-G. Kim and S. K. Park, *ACS Appl. Mater. Interfaces*, 2017, **9**, 26191–26200.
33 Y. H. Kim, C. Sachse, M. L. Machala, C. May, L. Müller-Meskamp and K. Leo, *Adv. Funct. Mater.*, 2011, **21**, 1076–1081.
34 J. Du, S. Pei, L. Ma and H.-M. Cheng, *Adv. Mater.*, 2014, **26**, 1958–1991.
35 B. Dan, G. C. Irvin and M. Pasquali, *ACS Nano*, 2009, **3**, 835–843.
36 J. O. Hwang, J. S. Park, D. S. Choi, J. Y. Kim, S. H. Lee, K. E. Lee, Y.-H. Kim, M. H. Song, S. Yoo and S. O. Kim, *ACS Nano*, 2012, **6**, 159–167.
37 J. Lee, S. Lee, G. Li, M. A. Petruska, D. C. Paine and S. Sun, *J. Am. Chem. Soc.*, 2012, **134**, 13410–13414.
38 J. Song, S. A. Kulinich, J. Li, Y. Liu and H. Zeng, *Angew. Chem.*, 2015, **127**, 472–476.
39 R. R. Da Silva, M. Yang, S.-I. Choi, M. Chi, M. Luo, C. Zhang, Z.-Y. Li, P. H. C. Camargo, S. J. L. Ribeiro and Y. Xia, *ACS Nano*, 2016, **10**, 7892–7900.
40 D. Zhang, R. Wang, M. Wen, D. Weng, X. Cui, J. Sun, H. Li and Y. Lu, *J. Am. Chem. Soc.*, 2012, **134**, 14283–14286.
41 J.-Y. Kim and N. A. Kotov, *Chem. Mater.*, 2014, **26**, 134–152.
42 B. H. Kim, C. M. Staller, S. H. Cho, S. Heo, C. E. Garrison, J. Kim and D. J. Milliron, *ACS Nano*, 2018, **12**, 3200–3208.
43 J. Lee, M. A. Petruska and S. Sun, *J. Phys. Chem. C*, 2014, **118**, 12017–12021.
44 Z. Chen, X. Qin, T. Zhou, X. Wu, S. Shao, M. Xie and Z. Cui, *J. Mater. Chem. C*, 2015, **3**, 11464–11470.
45 B. Bob, A. Machness, T.-B. Song, H. Zhou, C.-H. Chung and Y. Yang, *Nano Res.*, 2016, **9**, 392–400.
46 T. Yamada, K. Fukuhara, K. Matsuoka, H. Minemawari, J. Tsutsumi, N. Fukuda, K. Aoshima, S. Arai, Y. Makita, H. Kubo, T. Enomoto, T. Togashi, M. Kurihara and T. Hasegawa, *Nat. Commun.*, 2016, **7**, 11402.
47 T. Nishimura, N. Ito, K. Kinoshita, M. Matsukawa, Y. Imura and T. Kawai, *Small*, 2020, **16**, 1903365.
48 T.-B. Song, Y. Chen, C.-H. Chung, Y. Yang, B. Bob, H.-S. Duan, G. Li, K.-N. Tu, Y. Huang and Y. Yang, *ACS Nano*, 2014, **8**, 2804–2811.
49 C. Hwang, J. An, B. D. Choi, K. Kim, S.-W. Jung, K.-J. Baeg, M.-G. Kim, K. M. Ok and J. Hong, *J. Mater. Chem. C*, 2016, **4**, 1441–1447.
50 D. Lanigan and E. Thimsen, *ACS Nano*, 2016, **10**, 6744–6752.
51 C. F. Guo and Z. Ren, *Mater. Today*, 2015, **18**, 143–154.
52 W. Gaynor, G. F. Burkhard, M. D. McGehee and P. Peumans, *Adv. Mater.*, 2011, **23**, 2905–2910.
53 Y. Kim, T. I. Ryu, K.-H. Ok, M.-G. Kwak, S. Park, N.-G. Park, C. J. Han, B. S. Kim, M. J. Ko, H. J. Son and J.-W. Kim, *Adv. Funct. Mater.*, 2015, **25**, 4580–4589.
54 S. Kim, S. J. Lee, S. Cho, S. Shin, U. Jeong and J.-M. Myoung, *Chem. Commun.*, 2017, **53**, 8292–8295.
55 E. Lee, J. Ahn, H.-C. Kwon, S. Ma, K. Kim, S. Yun and J. Moon, *Adv. Energy Mater.*, 2018, **8**, 1702182.
56 Y. Won, A. Kim, D. Lee, W. Yang, K. Woo, S. Jeong and J. Moon, *NPG Asia Mater.*, 2014, **6**, e105.
57 Y. Ge, X. Duan, M. Zhang, L. Mei, J. Hu, W. Hu and X. Duan, *J. Am. Chem. Soc.*, 2018, **140**, 193–199.
58 X. Zhu, J. Xu, F. Qin, Z. Yan, A. Guo and C. Kan, *Nanoscale*, 2020, **12**, 14589–14597.
59 Y. Ko, M. Kwon, W. K. Bae, B. Lee, S. W. Kee and J. Cho, *Nat. Commun.*, 2017, **8**, 536.
60 D. Shin, C. H. Kwon, Y. Ko, B. Lee, S. W. Lee and J. Cho, *J. Mater. Chem. A*, 2018, **6**, 20421–20432.
61 Y. Ko, M. Kwon, Y. Song, S. W. Lee and J. Cho, *Adv. Funct. Mater.*, 2018, **28**, 1804926.
62 S. Cong, Y. Tian, Q. Li, Z. Zhao and F. Geng, *Adv. Mater.*, 2014, **26**, 4260–4267.

63 S. Heo, J. Kim, G. K. Ong and D. J. Milliron, *Nano Lett.*, 2017, **17**, 5756–5761.
64 V. Augustyn, P. Simon and B. Dunn, *Energy Environ. Sci.*, 2014, **7**, 1597–1614.
65 J.-L. Wang, Y.-R. Lu, H.-H. Li, J.-W. Liu and S.-H. Yu, *J. Am. Chem. Soc.*, 2017, **139**, 9921–9926.
66 Z.-S. Wu, G. Zhou, L.-C. Yin, W. Ren, F. Li and H.-M. Cheng, *Nano Energy*, 2012, **1**, 107–131.
67 Y. Ko, D. Shin, B. Koo, S. W. Lee, W.-S. Yoon and J. Cho, *Nano Energy*, 2015, **12**, 612–615.
68 C.-K. Lin, S.-C. Tseng, C.-H. Cheng, C.-Y. Chen and C.-C. Chen, *Thin Solid Films*, 2011, **520**, 1375–1378.
69 J. Kao, K. Thorkelsson, P. Bai, B. J. Rancatore and T. Xu, *Chem. Soc. Rev.*, 2013, **42**, 2654–2678.
70 Y. Ko, H. Baek, Y. Kim, M. Yoon and J. Cho, *ACS Nano*, 2013, **7**, 143–153.
71 M. Park, Y. Kim, Y. Ko, S. Cheong, S. W. Ryu and J. Cho, *J. Am. Chem. Soc.*, 2014, **136**, 17213–17223.
72 S. Cheong, J.-K. Kim and J. Cho, *Nanoscale*, 2016, **8**, 18315–18325.
73 I. Cho, H. Jung, B. G. Jeong, J. H. Chang, Y. Kim, K. Char, D. C. Lee, C. Lee, J. Cho and W. K. Bae, *ACS Nano*, 2017, **11**, 684–692.
74 C. H. Kwon, Y. Ko, D. Shin, M. Kwon, J. Park, W. K. Bae, S. W. Lee and J. Cho, *Nat. Commun.*, 2018, **9**, 4479.
75 Y. Song, D. Kim, S. Kang, Y. Ko, J. Ko, J. Huh, Y. Ko, S. W. Lee and J. Cho, *Adv. Funct. Mater.*, 2019, **29**, 1806584.
76 S. Kang, D. Nam, J. Choi, J. Ko, D. Kim, C. H. Kwon, J. Huh and J. Cho, *ACS Appl. Mater. Interfaces*, 2019, **11**, 12032–12042.
77 S. Lee, Y. Song, Y. Ko, Y. Ko, J. Ko, C. H. Kwon, J. Huh, S.-W. Kim, B. Yeom and J. Cho, *Adv. Mater.*, 2020, **32**, 1906460.
78 D. Huo, M. J. Kim, Z. Lyu, Y. Shi, B. J. Wiley and Y. Xia, *Chem. Rev.*, 2019, **119**, 8972–9073.
79 L. Hu, H. S. Kim, J.-Y. Lee, P. Peumans and Y. Cui, *ACS Nano*, 2010, **4**, 2955–2963.
80 A. R. Rathmell and B. J. Wiley, *Adv. Mater.*, 2011, **23**, 4798–4803.
81 R. M. Mutiso, M. C. Sherrott, A. R. Rathmell, B. J. Wiley and K. I. Winey, *ACS Nano*, 2013, **7**, 7654–7663.
82 T. Sannicolo, M. Lagrange, A. Cabos, C. Celle, J.-P. Simonato and D. Bellet, *Small*, 2016, **12**, 6052–6075.
83 Y. Sun, B. Mayers, T. Herricks and Y. Xia, *Nano Lett.*, 2003, **3**, 955–960.
84 J. Jiu, T. Araki, J. Wang, M. Nogi, T. Sugahara, S. Nagao, H. Koga, K. Suganuma, E. Nakazawa, M. Hara, H. Uchida and K. Shinozaki, *J. Mater. Chem. A*, 2014, **2**, 6326–6330.
85 B. Li, S. Ye, I. E. Stewart, S. Alvarez and B. J. Wiley, *Nano Lett.*, 2015, **15**, 6722–6726.
86 K. M. Koczkur, S. Mourdikoudis, L. Polavarapu and S. E. Skrabalak, *Dalton Trans.*, 2015, **44**, 17883–17905.
87 Y. Ge, J. Liu, X. Liu, J. Hu, X. Duan and X. Duan, *J. Am. Chem. Soc.*, 2019, **141**, 12251–12257.
88 H. Wang, H. Tang, J. Liang and Y. Chen, *Adv. Funct. Mater.*, 2018, **28**, 1804479.
89 M. Lagrange, D. P. Langley, G. Giusti, C. Jiménez, Y. Bréchet and D. Bellet, *Nanoscale*, 2015, **7**, 17410–17423.
90 E. C. Garnett, W. Cai, J. J. Cha, F. Mahmood, S. T. Connor, M. G. Christoforo, Y. Cui, M. D. McGehee and M. L. Brongersma, *Nat. Mater.*, 2012, **11**, 241–249.
91 J. Jang, B. G. Hyun, S. Ji, E. Cho, B. W. An, W. H. Cheong and J.-U. Park, *NPG Asia Mater.*, 2017, **9**, e432.
92 D. Kumar, V. Stoichkov, E. Brousseau, G. C. Smith and J. Kettle, *Nanoscale*, 2019, **11**, 5760–5769.
93 Y. Fang, Z. Wu, J. Li, F. Jiang, K. Zhang, Y. Zhang, Y. Zhou, J. Zhou and B. Hu, *Adv. Funct. Mater.*, 2018, **28**, 1705409.
94 M. Grouchko, P. Roitman, X. Zhu, I. Popov, A. Kamyshny, H. Su and S. Magdassi, *Nat. Commun.*, 2014, **5**, 2994.
95 M. Grouchko, A. Kamyshny, C. F. Mihailescu, D. F. Anghel and S. Magdassi, *ACS Nano*, 2011, **4**, 3354–3359.
96 M. S. Kang, H. Joh, H. Kim, H.-W. Yun, D. Kim, H. K. Woo, W. S. Lee, S.-H. Hong and S. J. Oh, *Nanoscale*, 2018, **10**, 18415–18422.
97 H. Sim, C. Kim, S. Bok, M. K. Kim, H. Oh, G.-H. Lim, S. M. Cho and B. Lim, *Nanoscale*, 2018, **10**, 12087–12092.
98 A. T. Fafarman, S.-H. Hong, S. J. Oh, H. Caglayan, X. Ye, B. T. Diroll, N. Engheta, C. B. Murray and C. R. Kagan, *ACS Nano*, 2014, **8**, 2746–2754.
99 A. Dong, X. Ye, J. Chen, Y. Kang, T. Gordon, J. M. Kikkawa and C. B. Murray, *J. Am. Chem. Soc.*, 2011, **133**, 998–1006.
100 S. Heo, A. Agrawal and D. J. Milliron, *Adv. Funct. Mater.*, 2019, **29**, 1904555.
101 M. V. Kovalenko, M. Scheele and D. V. Talapin, *Science*, 2009, **12**, 1417–1420.
102 G. S. Perera, S. M. Ansar, S. Hu, M. Chen, S. Zou, C. U. Pittman and D. Zhang, *J. Phys. Chem. C*, 2014, **118**, 10509–10518.
103 A. Dong, Y. Jiao and D. J. Milliron, *ACS Nano*, 2013, **7**, 10978–10984.
104 B. M. Crockett, A. W. Jansons, K. M. Koskela, M. C. Sharps, D. W. Johnson and J. E. Hutchison, *Chem. Mater.*, 2019, **31**, 3370–3378.
105 M. H. Zarghami, Y. Liu, M. Gibbs, E. Gebremichael, C. Webster and M. Law, *ACS Nano*, 2010, **4**, 2475–2485.
106 F.-X. Xiao, M. Pagliaro, Y.-J. Xu and B. Liu, *Chem. Soc. Rev.*, 2016, **45**, 3088–3121.
107 S. Srivastava and N. A. Kotov, *Acc. Chem. Res.*, 2008, **41**, 1831–1841.
108 Q. An, T. Huang and F. Shi, *Chem. Soc. Rev.*, 2018, **47**, 5061–5098.
109 G. Decher, *Science*, 1997, **277**, 1232–1237.
110 Y. Kim, J. Zhu, B. Yeom, M. D. Prima, X. Su, J.-G. Kim, S. J. Yoo, C. Uher and N. A. Kotov, *Nature*, 2013, **500**, 59–64.
111 J.-S. Lee, J. Cho, C. Lee, I. Kim, J. Park, Y.-M. Kim, H. Shin, J. Lee and F. Caruso, *Nat. Nanotechnol.*, 2007, **2**, 790–795.
112 S. Y. Kim, J. Hong, R. Kavian, S. W. Lee, M. N. Hyder, Y. Shao-Horn and P. T. Hammond, *Energy Environ. Sci.*, 2013, **6**, 888–897.

113 B. S. Shim, J. Zhu, E. Jan, K. Critchley and N. A. Kotov, *ACS Nano*, 2010, **4**, 3725–3734.
114 D. W. Lee, T.-K. Hong, D. Kang, J. Lee, M. Heo, J. Y. Kim, B.-S. Kim and H. S. Shin, *J. Mater. Chem.*, 2011, **21**, 3438–3442.
115 C. Kim, H. An, A. Jung and B. Yeom, *J. Colloid Interface Sci.*, 2017, **493**, 371–377.
116 T.-K. Hong, D. W. Lee, H. J. Choi, H. S. Shin and B.-S. Kim, *ACS Nano*, 2010, **4**, 3861–3868.
117 B. T. Camic, F. Oytun, M. H. Aslan, H. J. Shin, H. Choi and F. Basarir, *J. Colloid Interface Sci.*, 2017, **505**, 79–86.
118 F. Oytun, V. Kara, O. Alpturk and F. Basarir, *Thin Solid Films*, 2017, **636**, 40–47.
119 S. J. Lee, Y. R. Lim, S. Ji, S. K. Kim, Y. Yoon, W. Song, S. Myung, J. Lim, K.-S. An, J.-S. Park and S. S. Lee, *Carbon*, 2018, **126**, 241–246.
120 J. Yun, *Adv. Funct. Mater.*, 2017, **27**, 1606641.
121 J. Schmitt, G. Decher, W. J. Dressick, S. K. Brandow, R. E. Geer, R. Shashidhar and J. M. Calvert, *Adv. Mater.*, 1997, **9**, 61–65.
122 C. Peng, Y. S. Thio and R. A. Gerhardt, *J. Phys. Chem. C*, 2010, **114**, 9685–9692.
123 I. Cho, Y. Song, S. Cheong, Y. Kim and J. Cho, *Small*, 2020, **16**, 1906768.
124 J. Choi, D. Nam, D. Shin, Y. Song, C. H. Kwon, I. Cho, S. W. Lee and J. Cho, *ACS Nano*, 2019, **13**, 12719–12731.
125 J. Yun, Y. Song, I. Cho, Y. Ko, C. H. Kwon and J. Cho, *Nanoscale*, 2019, **11**, 17815–17830.
126 Y. Wang, W. Zhou, Q. Kang, J. Chen, Y. Li, X. Feng, D. Wang, Y. Ma and W. Huang, *ACS Appl. Mater. Interfaces*, 2018, **10**, 27001–27008.
127 S. B. Singh, T. I. Singh, N. H. Kim and J. H. Lee, *J. Mater. Chem. A*, 2019, **7**, 10672–10683.
128 X. Y. Liu, Y. Q. Gao and G. W. Yang, *Nanoscale*, 2016, **8**, 4227–4235.
129 C. Zhang, T. M. Higgins, S.-H. Park, S. E. O'Brien, D. Long, J. N. Coleman and V. Nicolosi, *Nano Energy*, 2016, **28**, 495–505.
130 X. Huang, H. Zhang and N. Li, *Nanotechnology*, 2017, **28**, 075402.
131 S. Bellani, L. Najafi, G. Tullii, A. Ansaldo, R. Oropesa-Nuñez, M. Prato, M. Colombo, M. R. Antognazza and F. Bonaccorso, *J. Mater. Chem. A*, 2017, **5**, 25177–25186.
132 S. Zhang, Y. Li, T. Zhang, S. Cao, Q. Yao, H. Lin, H. Ye, A. Fisher and J. Y. Lee, *ACS Appl. Mater. Interfaces*, 2019, **11**, 48062–48070.
133 B. C. Mei, K. Susumu, I. L. Medintz and H. Mattoussi, *Nat. Protoc.*, 2009, **4**, 412–423.
134 S. Cong, F. Geng and Z. Zhao, *Adv. Mater.*, 2016, **28**, 10518–10528.
135 H. Fang, P. Zheng, R. Ma, C. Xu, G. Yang, Q. Wang and H. Wang, *Mater. Horiz.*, 2018, **5**, 1000–1007.
136 H. Li, L. McRae and A. Y. Elezzabi, *ACS Appl. Mater. Interfaces*, 2018, **10**, 10520–10527.
137 A. Azam, J. Kim, J. Park, T. G. Novak, A. P. Tiwari, S. H. Song, B. Kim and S. Jeon, *Nano Lett.*, 2018, **18**, 5646–5651.
138 K. Fujimoto, S. Fujita, B. Ding and S. Shiratori, *Jpn. J. Appl. Phys.*, 2005, **44**, L126–L128.
139 K. C. Krogman, R. E. Cohen, P. T. Hammond, M. F. Rubner and B. N. Wang, *Bioinspiration Biomimetics*, 2013, **8**, 045005.